Electronic Supplementary Information

Highly Porous, Low Band-gap $Ni_xMn_{3-x}O_4$ (0.55 ≤ x ≤ 1.2) Spinel Nanoparticles with In-situ Coated Carbon as Advanced Cathode Materials for Zinc-ion Batteries

Jun Long[ab], Jinxing Gu[c], Zhanhong Yang[a*], Jianfeng Mao[b], Junnan Hao[b], Zhongfang

Chen[c*], Zaiping Guo[bd*]

[a]Hunan Provincial Key Laboratory of Chemical Power Sources, College of Chemistry and Chemical Engineering, Central South University, Changsha 410083, P. R. China

[b]Institute for Superconducting & Electronic Materials, University of Wollongong, Wollongong, New South Wales 2522, Australia

[c]Department of Chemistry, Institute for Functional Nanomaterials, University of Puerto Rico Rio, Rio Piedras Campus, San Juan, PR 00931, USA.

[d]School of Mechanical, Materials, Mechatronics and Biomedical Engineering, University of Wollongong, Wollongong, New South Wales 2500, Australia

[*]Corresponding author:

Dr. & Prof. Zhanhong Yang. Email: zhyang@csu.edu.cn

Dr. & Prof. Zaiping Guo. Email: zguo@uow.edu.au

Dr. & Prof. Zhongfang Chen. Email: zhongfangchen@gmail.coom

Experimental Section

Materials characterization. X-ray diffraction (XRD) data were obtained on a GBC MMA X-ray diffractometer with a Cu-Kα1 source (λ = 1.5418 Å) operated at 40 kV to investigate the crystal structure of each sample. Scanning electron microscopy (SEM) was conducted on a Helios Navo NanoSEM230 and a field-emission scanning electron microscopy (JEOL-7500). The detailed microstructure of samples was characterized by a transmission electron microscopy (Titan G2 60-300) with an accelerating voltage of 300 kV. The specific surface area and pore size distribution of the samples were calculated by the Brunauer-Emmett-Teller (BET) and Barrett-Joyner-Halenda (BJH) models from N_2 adsorption isotherms at 77 K (JW-BK132F, Beijing). The presence of different modes of vibrations of the metal oxides was investigated using a Fourier transform infrared spectrophotometer (FTIR, AVTA-TAR, 370) over the range from 400 to 4,000 cm^{-1} with a resolution of 2 cm^{-1}. Raman spectroscopy measurements of samples were obtained using a LabRAM Hr800 confocal Raman microscope system. Thermogravimetric (TG) analysis was implemented by using a Mettler-Toledo thermogravimetric analyzer TGA/DSC1 System to ascertain the changes in weight of the hybrids with increasing temperature and to evaluate the amount of carbon in the compounds. The contents of transition metals (Ni and Mn) in $Ni_xMn_{3-x}O_4@C$ were determined by an inductively coupled plasma – atomic emission spectrometer (ICP-AES, Shimadzu). The as-prepared $Ni_xMn_{3-x}O_4@C$ samples were first immersed and dissolved in HNO_3 solution (3 M) for 30 h, and after that, analyzed by the ICP-AES instrument. X-ray photoelectron spectroscopy (XPS) measurements were carried out with an XPS spectrometer (Kα radiation, 1486.8 eV) for

detecting the bonding configuration and the surface element composition of the obtained samples.

Electrochemical measurements. Electrochemical performances were evaluated in CR3032 coin cells. The zinc half-cell consisted of a zinc foil disk as the counter electrode, aqueous 3 M $ZnSO_4$ with 0.15 M $MnSO_4$ as the electrolyte, glass fiber as the separator, and the obtained active materials as the working electrode. The cathode electrode was prepared by mixing the $Ni_xMn_{3-x}O_4@C$ product, Super P, and polytetrafluoroethylene (the binder) in the weight ratio of 7:2:1. Then, the obtained homogeneous slurry was compressed onto a steel grid (about 20 MPa) followed by drying under vacuum at 80 °C for 12h. The corresponding mass of active materials on each steel grid disk was ~1.5 mg cm^{-2}, while the zinc foil disk had loading of ~15 mg cm^{-2}, which can eliminate the effect of zinc fading during discharge/charge. Galvanostatic charge/discharge and rate tests were performed on Neware battery testing equipment (BTS-4000) within a voltage window of 1.0-1.85 V. The tested current density and the corresponding specific capacity are based on the mass of $Ni_xMn_{3-x}O_4@C$ in each electrode. Cyclic voltammetry (CV) tests were carried out using a CH Instruments electrochemical workstation at various scan rates within the potential window of 1.0-1.85 V. Electrochemical impedance spectroscopy (EIS) tests were also conducted using a CH Instruments electrochemical workstation (AC amplitude of 5 mV) in the frequency range from 100 kHz to 10 mHz.

Computational Methods. The spin-unrestricted density functional theory (DFT) [1] with the projector-augmented-wave method [2, 3] implemented in the Vienna *ab initio* simulation package (VASP) [4, 5] was adopted for all the calculations, including structural

relaxation and density of states (DOS) calculations. The generalized gradient approximation plus Hubbard potential correction (GGA+U) method was utilized because electrons in d orbitals of Ni and Mn elements have strong interactions with each other, where the exchange-correlation energy was dealt with using the Perdew, Burke, and Ernzerhof (PBE) functional [6]. The effective U values for Ni and Mn were selected as 6 and 5 eV, as reported by previous works [7]. A kinetic cutoff energy of 500 eV was used for structural relaxation. All atoms in the unit cell were fully relaxed with an energy convergence of 10^{-6} eV, as well as a force convergence of 0.01 eV/ Å.

The unit cell of the pure Mn_3O_4 contains six Mn ions, so that it has seven possible magnetic orderings: FM = (↑↑↑↑↑↑), FIM 1 = (↓↓↑↑↑↑), FIM 2 = (↑↓↑↑↑↑), FIM 3 = (↑↑↓↓↑↑), FIM 4 = (↑↑↑↓↑↓), FIM 5 = (↑↑↑↓↑↑) and FIM 6 = (↑↓↑↓↑↓) [8]. Our calculations found that the pure Mn_3O_4 exhibits slightly ferrimagnetism with the FIM 6 magnetic ordering. The magnetic moment of octahedrally-coordinated Mn ion is around 4.0 μ_B, while that of the tetrahedrally-coordinated Mn ion is around 4.6 μ_B. Upon doping Ni ion on the B-sites to generate $Ni_xMn_{3-x}O_4$, it becomes metallic in all the calculated cases. In the case of $NiMn_5O_8$ ($x = 0.5$), the Ni ion replaces one of the octahedral-coordinated Mn ions, exhibiting the magnetic ordering of (↓(Ni)↑↑↑↑↑). The calculated magnetic moments for Ni, Oct-Mn, and Tetra-Mn ions are 1.71, 4.03, and 4.49 μ_B, respectively. In case of $Ni_2Mn_4O_8$ (x = 1.0), two Ni ions replace the two Oct-Mn ions, exhibiting the magnetic ordering of (↓(Ni)↓(Ni)↑↑↑↑). The calculated magnetic moments for Ni, Oct-Mn, and Tetra-Mn ions are 1.72, 3.83, and 4.52 μ_B, respectively. In case of $Ni_2Mn_4O_8$ (x = 1.5), three Ni ions replace the three Oct-Mn ions, exhibiting the magnetic ordering of (

$\downarrow(Ni)\uparrow\uparrow\uparrow\uparrow\uparrow$). The calculated magnetic moments for Oct-Mn and Tetra-Mn ions are 3.60 and 4.49 μ_B, while the magnetic moments for Ni ions are 1.75 ($\downarrow$), 1.67, and 1.38 μ_B, respectively. The enriched magnetic moments of the $Ni_xMn_{3-x}O_4$ system endow the materials with unique electronic properties.
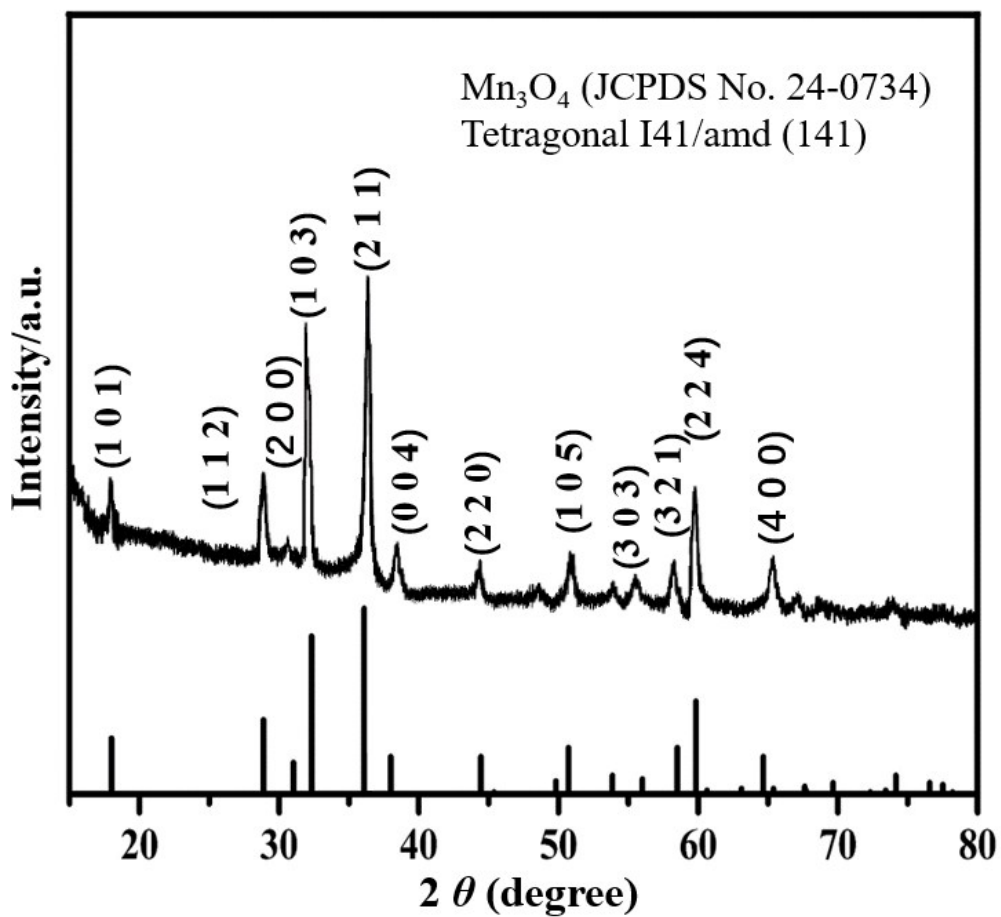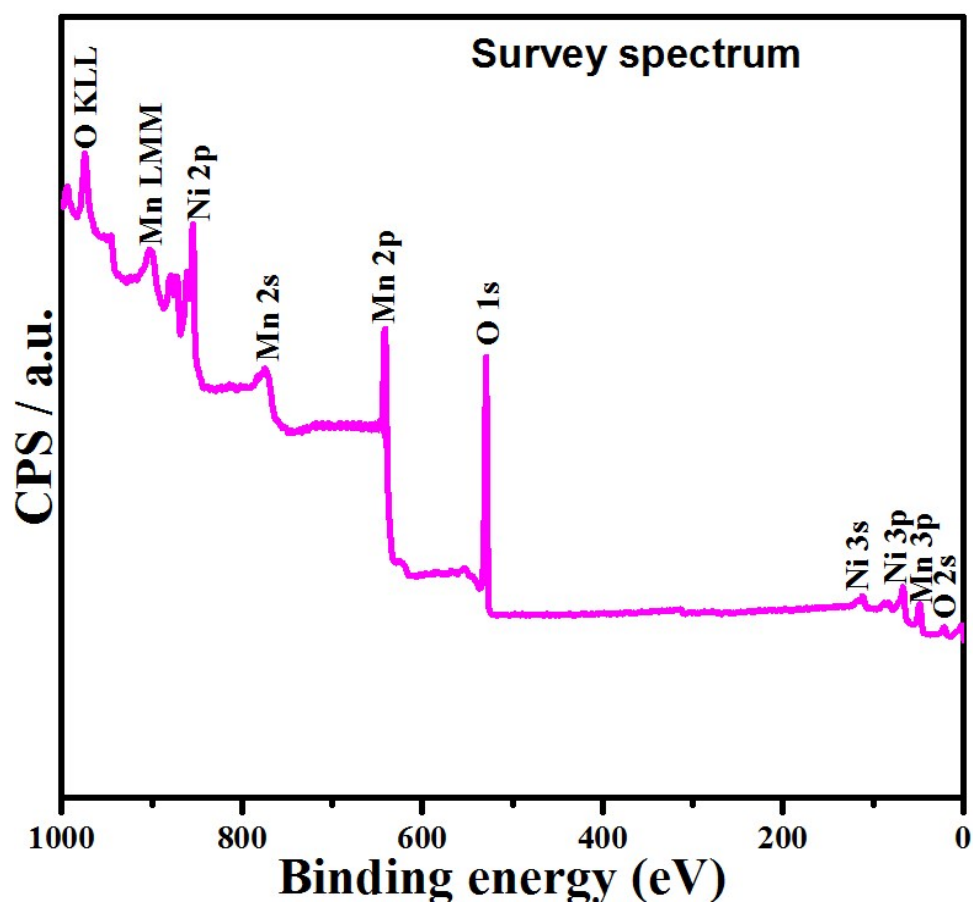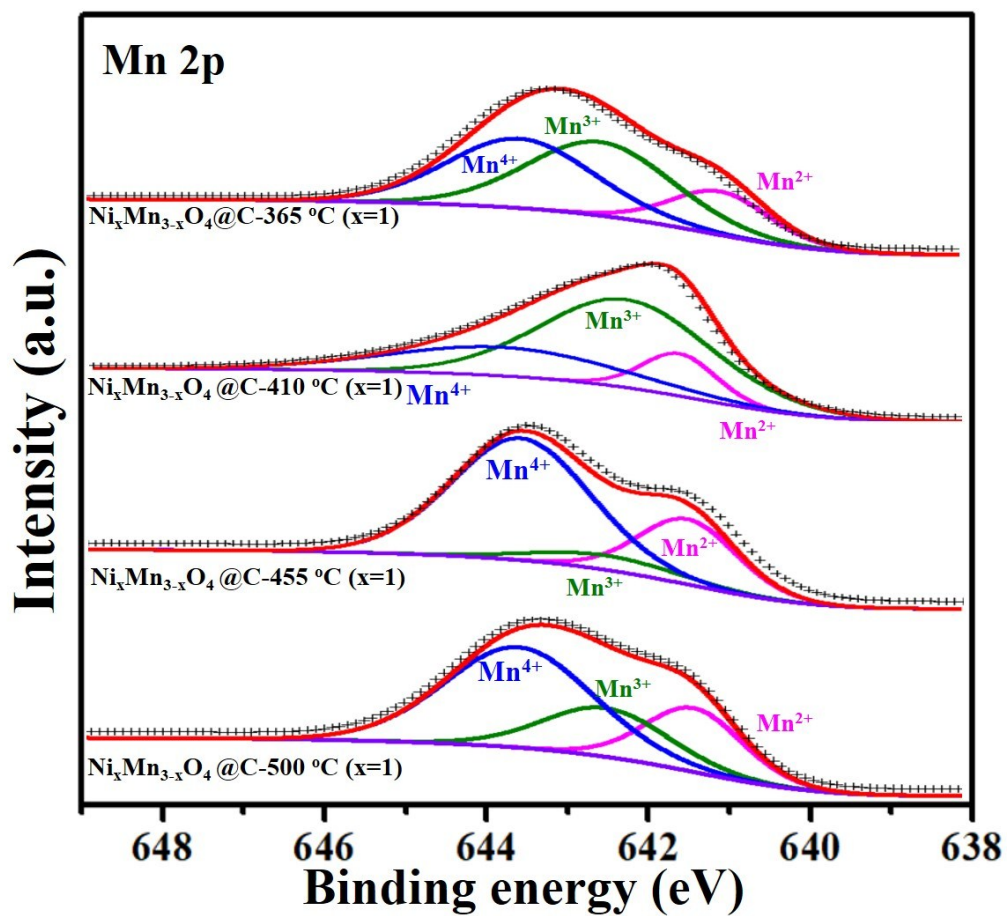
Figure S1. XRD pattern of $Ni_xMn_{3-x}O_4@C$ (x = 0).

Figure S2. XPS Survey spectrum of $Ni_xMn_{3-x}O_4$ (x = 1).

Figure S3. Mn 2p XPS spectra of samples of the precursor of $Ni_xMn_{3-x}O_4@C$ ($x = 1$) that were calcined in oxygen atmosphere in a tubular at different temperatures. As shown in the Figure S4, the obvious full width at half maximum (FWHM) of the Mn 2p signals indicates a multiplet splitting and charging effect due to the Mn^{4+}, Mn^{3+}, and Mn^{2+} ions [9]. Three peaks are assigned to the corresponding binding energies of 643.0-643.9 eV, 642.2-642.7 eV, and 641.0-641.7 eV, respectively. Notably, the peaks area belonging to Mn^{4+} 2p slightly increased and that of Mn^{3+} 2p diminished with increasing calcination temperature. Then, the peaks area belonging to Mn^{4+} 2p started to decline when the temperature exceeded 455 °C. Additionally, the peaks intensities (%) for the samples annealed at different calcination temperatures are shown in the Table S1, Supporting Information.
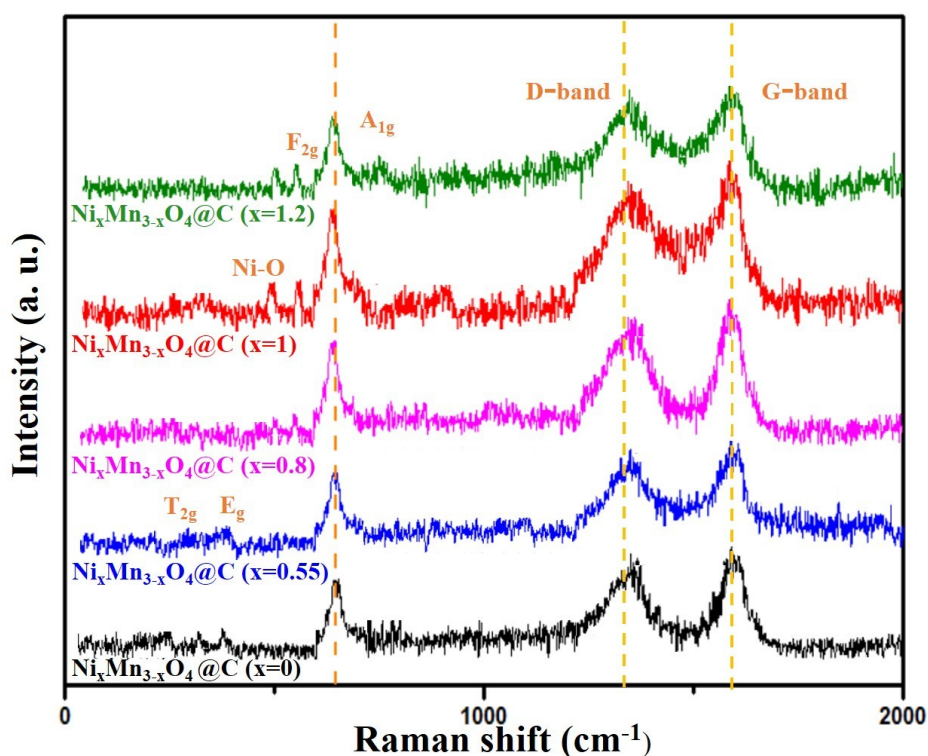

Figure S4. Raman spectra of $Ni_xMn_{3-x}O_4@C$ ($x = 0, 0.55, 0.8, 1, 1.2$) samples. It can be

seen that as more nickel is embedded in the structure, a slight shift of the A_{1g} Raman peaks toward lower frequencies is observed, which indicates that Ni^{2+} is incorporated into the lattice [10]. The typical carbon peaks located at 1362 cm^{-1} (D band) and 1580 cm^{-1} (G band) are also detected in the five samples.
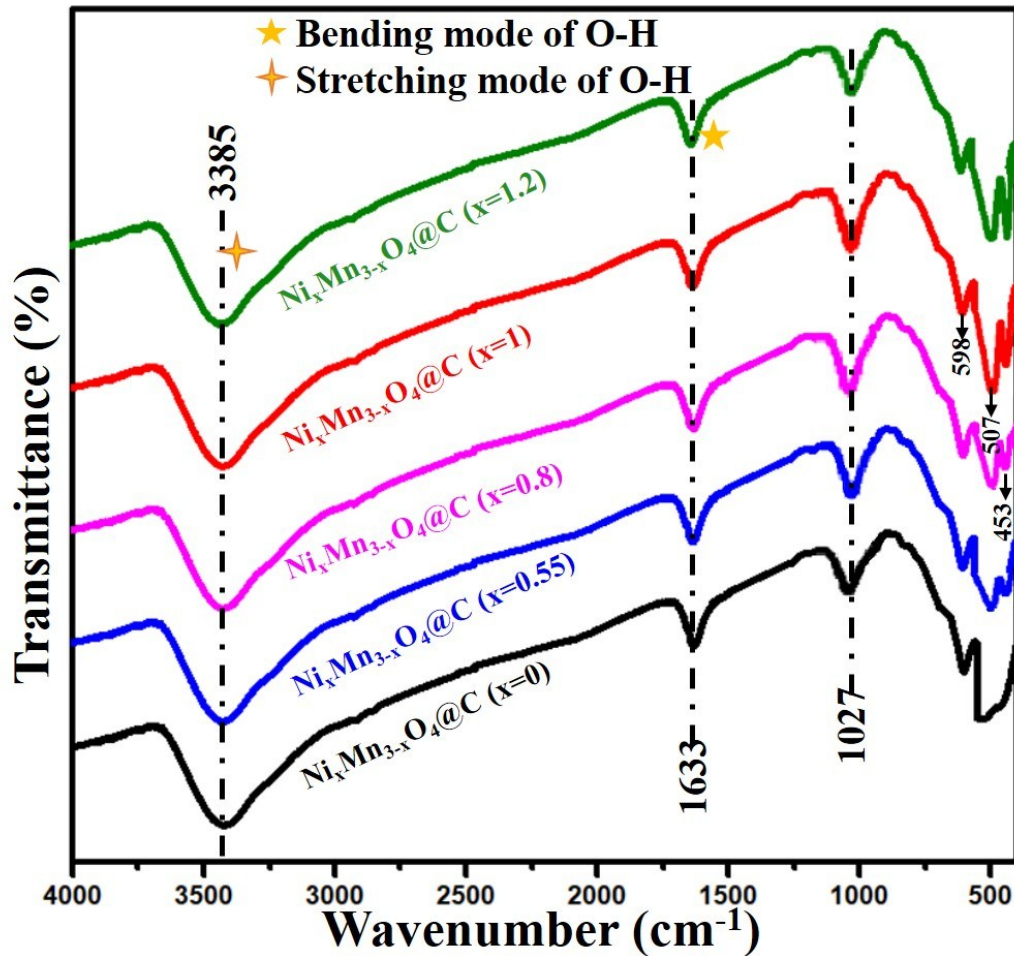
**Figure S5.** FTIR spectra of $Ni_xMn_{3-x}O_4@C$ ($x = 0, 0.55, 0.8, 1, 1.2$) samples. FTIR spectra are complementary Raman spectra (Figure S4), and thus provide the valuable information on the chemical bonds of Ni-Mn-O systems [11].
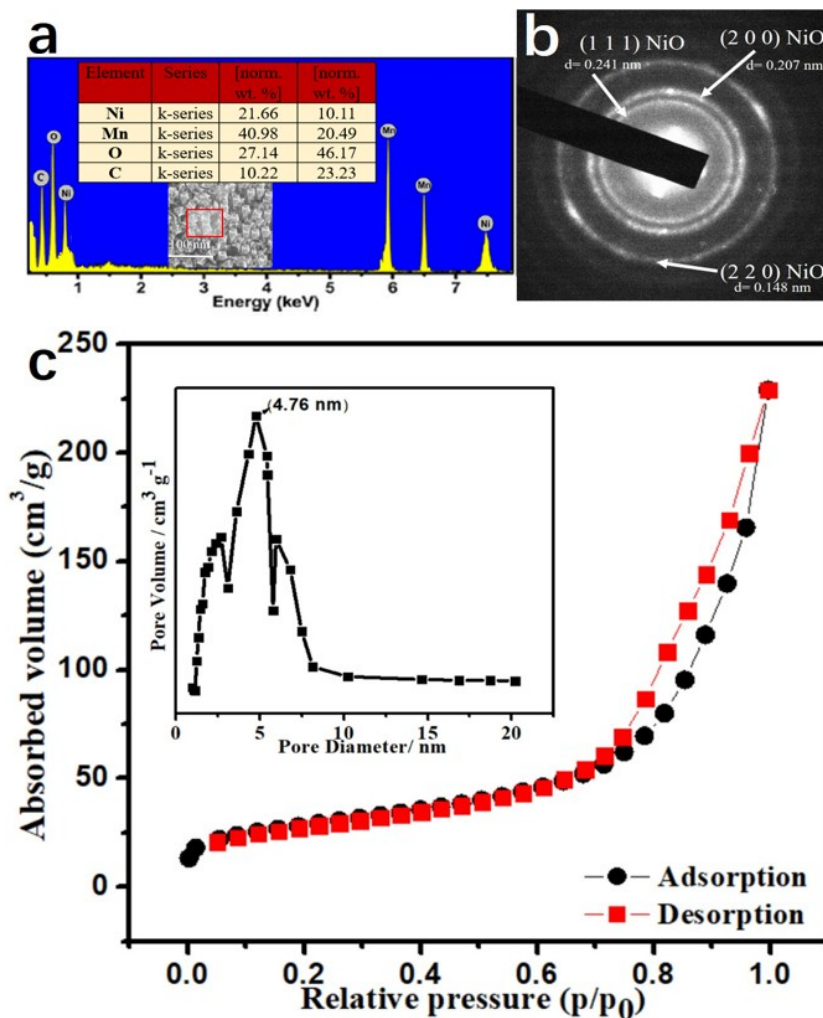
Figure S6. a) EDX spectrum of as-synthesized $Ni_xMn_{3-x}O_4@C$ (x = 1). The area in the red rectangle in the SEM image in the inset was used for EDX. b) SAED pattern of $Ni_xMn_{3-x}O_4@C$ (x = 1.2). c) Nitrogen adsorption/desorption isotherms of $Ni_xMn_{3-x}O_4@C$ (x = 1) nanoparticles (with the inset showing the corresponding Barrett-Joyner-Halenda (BJH) pore size distribution curve for the sample).
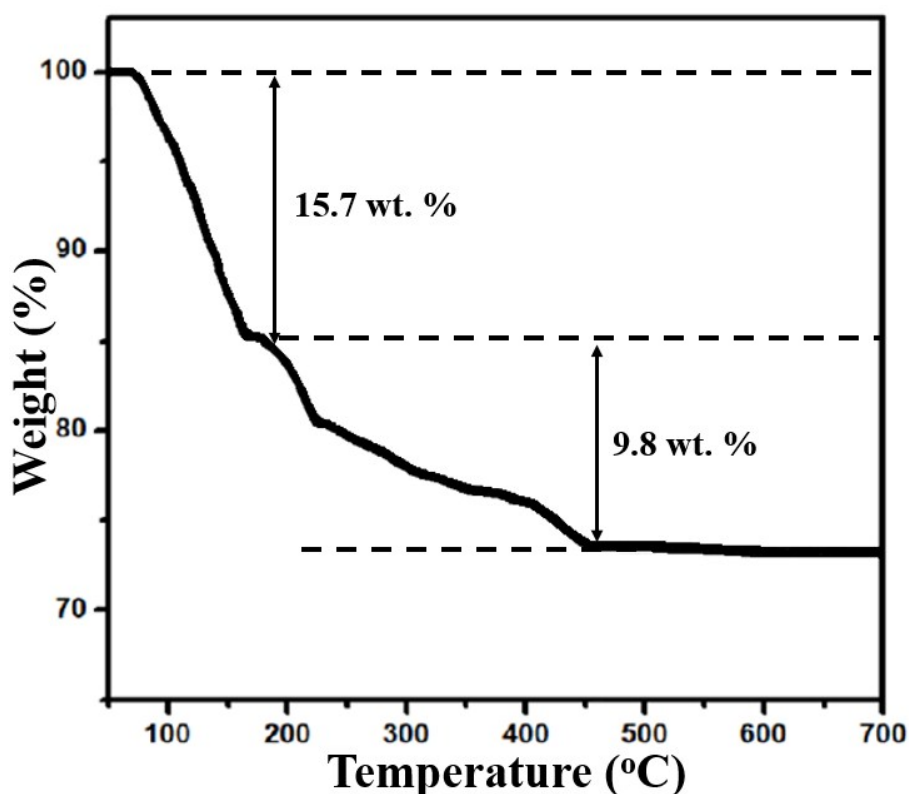

Figure S7. TG analysis of $Ni_xMn_{3-x}O_4@C$ (x = 1). The weight loss (~9.8%) between 200 °C and 450 °C is due to the loss of the carbon-coating layer on the surface of the nanoparticles. While the weight loss (~15.7%) below 200 °C is owing to the elimination of adsorbed water.
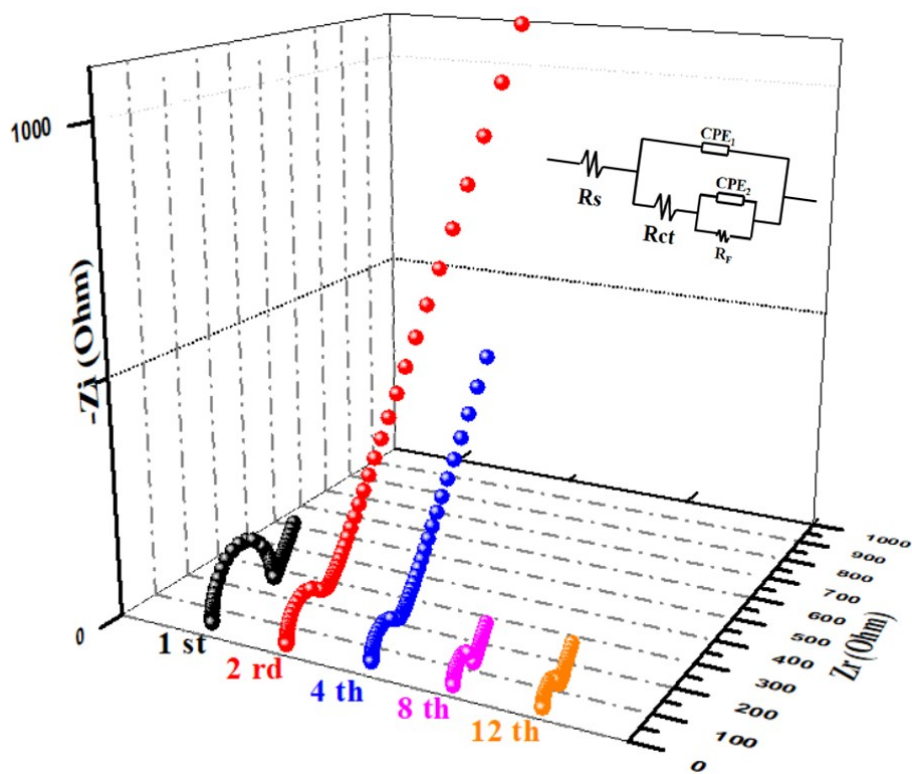
Figure S8. EIS spectra of $Ni_xMn_{3-x}O_4@C$ ($x = 1$) electrode after the 1st, 2nd, 4th, 8th, and 12th discharge in (2 M $ZnSO_4$ + 0.15 M $MnSO_4$). The inset is the equivalent circuit for fitting the impedance spectra. The impedance becomes smaller as cycling continues because of the increasing surface area of the active material [12]. The impedance

decreases in the course of cycling owing to the enhanced electrode performance, which can be used to prove the initial activation process of the tested electrode. The equivalent circuit consists of Rs (bulk solution resistance), a constant phase element (CPE), a pseudocapacitive element Cp, the charge-transfer resistance Rct, and the film resistance R_F.
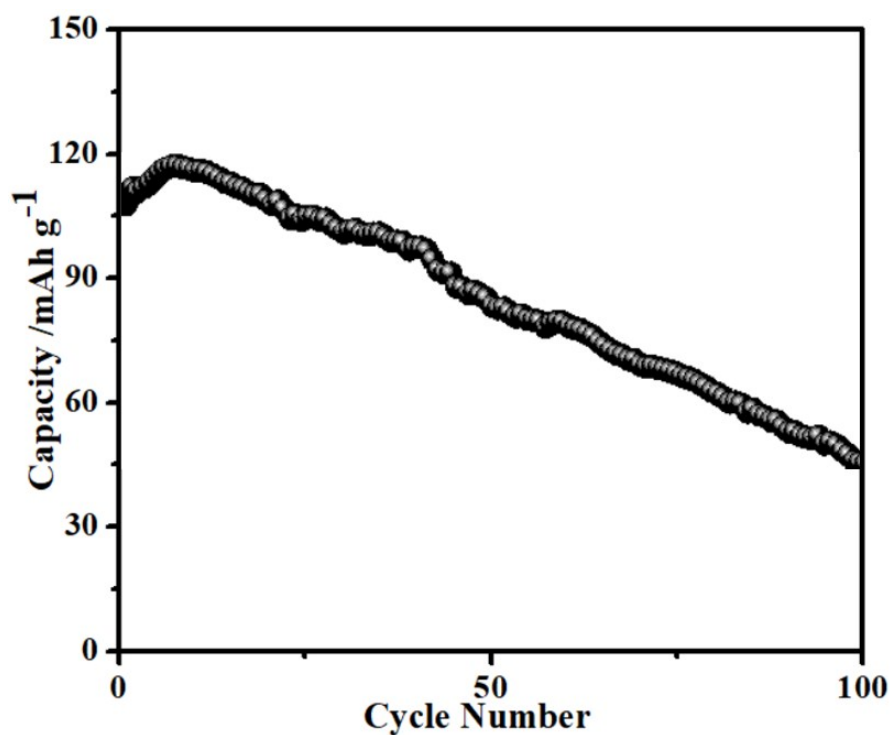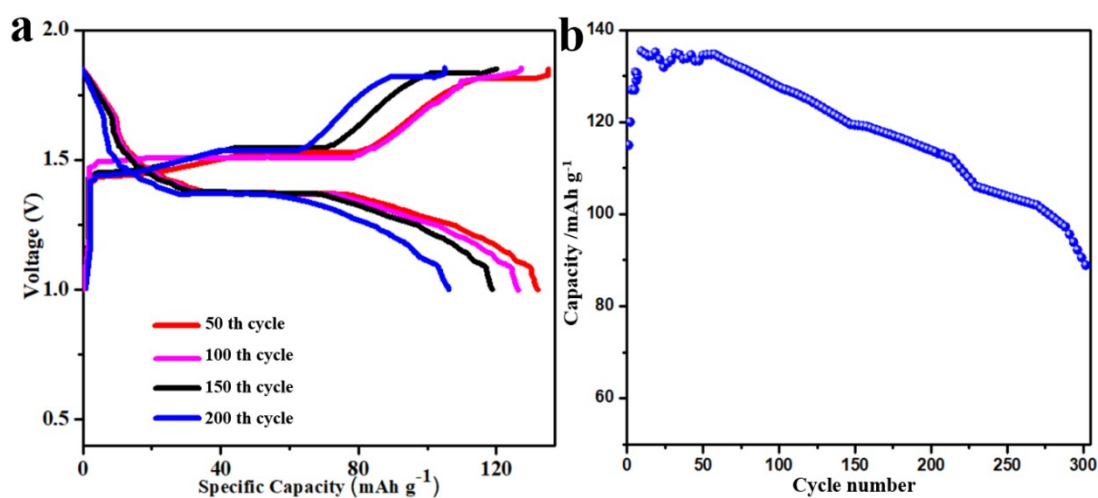

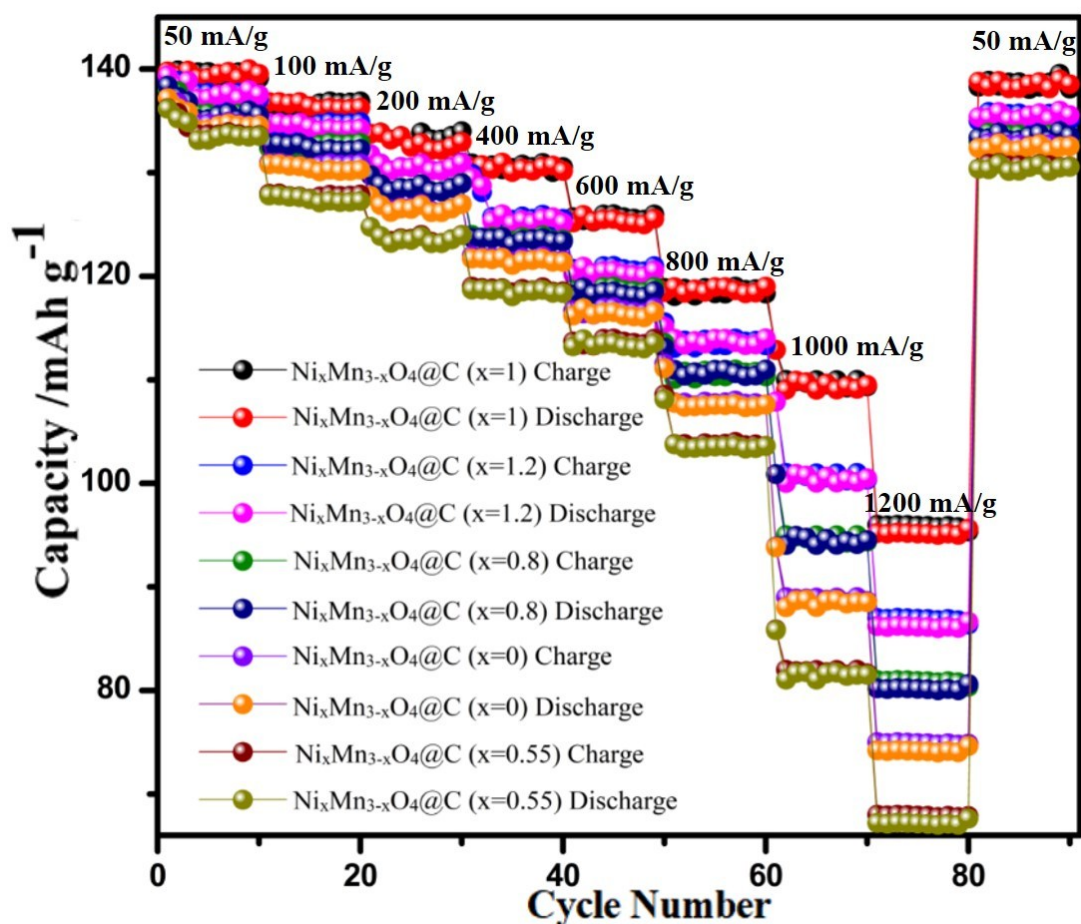**Figure S9.** Cycling performance of $Ni_xMn_{3-x}O_4$+ C ($x = 1$) mixture
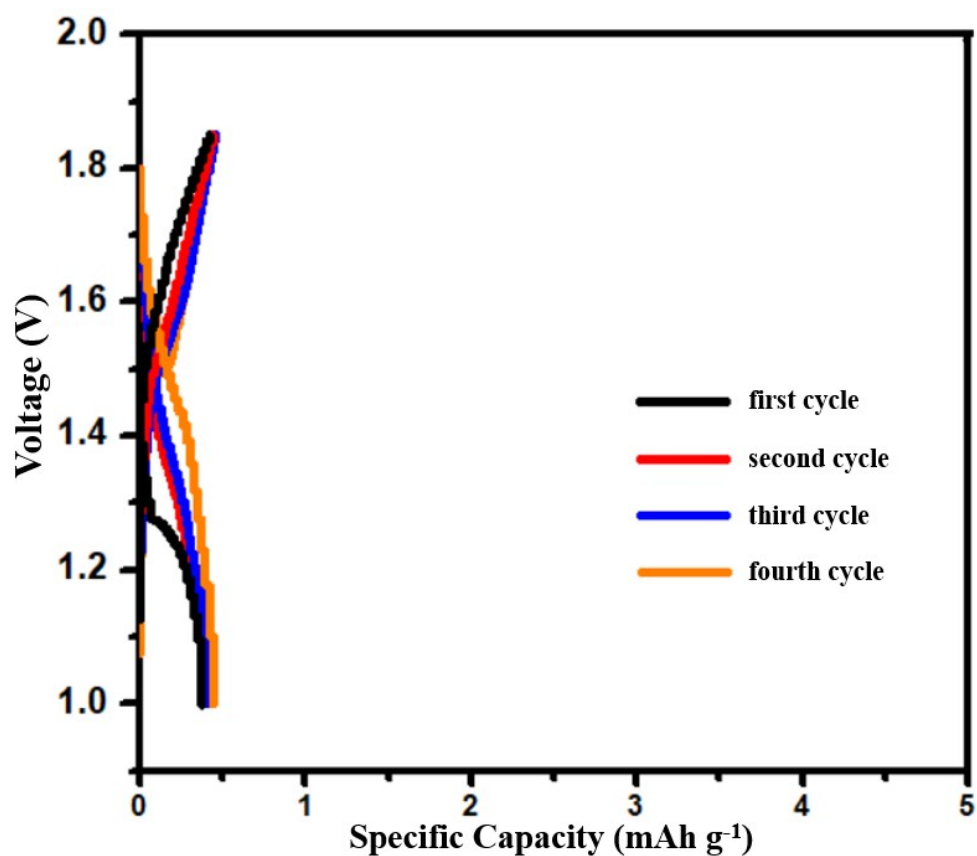
Figure S10. Charge/discharge profiles of the carbon at 5 mA g^{-1} in (2 M ZnSO$_4$ + 0.15 M MnSO$_4$). This carbon was synthesized by the same pyrolysis method at low temperature, which is consistent with the method for preparing Ni$_x$Mn$_{3-x}$O$_4$@C (x = 1), and which

shows amorphous phase. As shown in the Figure S10, it can deliver about 0.5 mAh g^{-1} even at a very low current density, indicating that the capacity from the carbon should be neglected for Ni$_x$Mn$_{3-x}$O$_4$@C (x = 1) during charge/discharge.
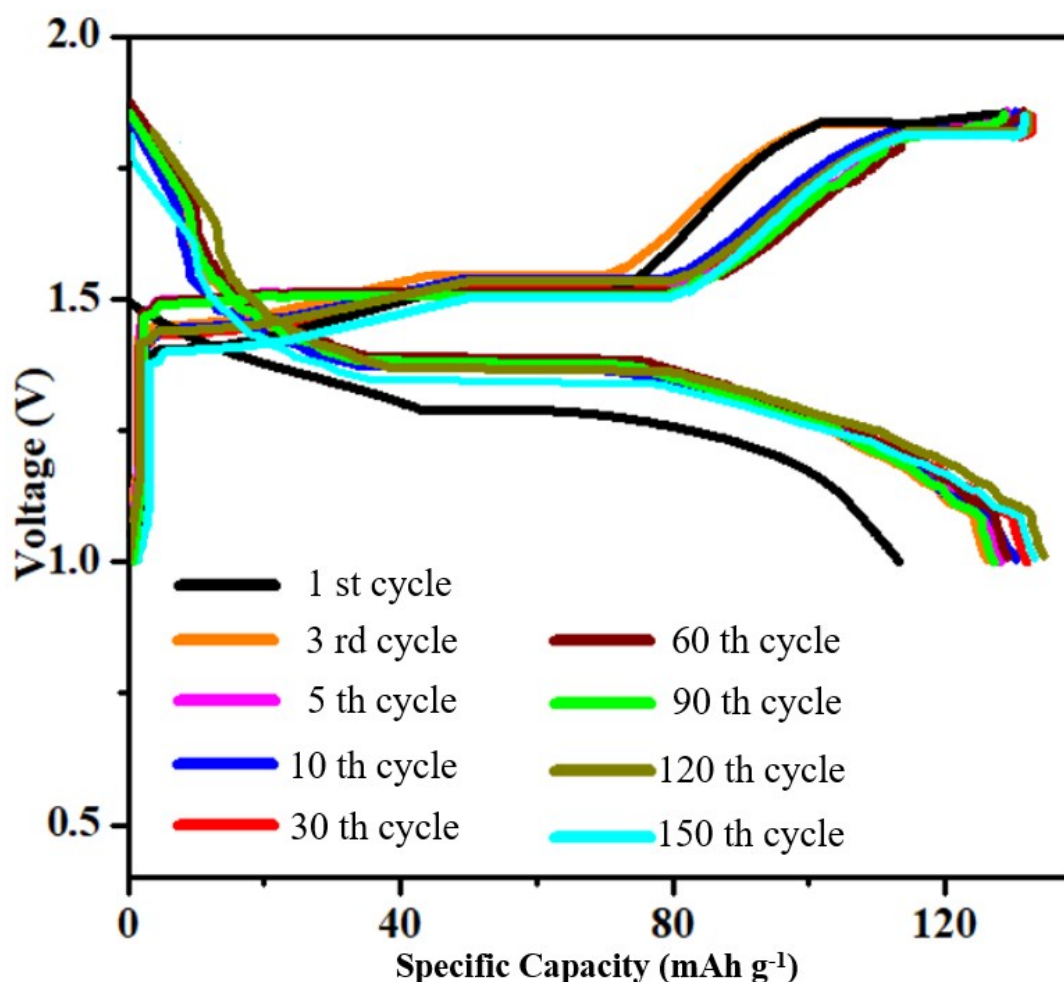

Figure S11. (a) Typical charge/discharge profiles and (b) cycling performance of Ni$_x$Mn$_{3-x}$O$_4$@C (x = 1) at 150 mA g^{-1} in 2 M ZnSO$_4$ electrolyte. To study the important synergistic effects of Mn^{2+} and Zn^{2+}, a coin cell was assembled under the same condition without Mn^{2+} additive in the electrolyte. As shown in the image above, the capacity drops rapidly, and there is a lower coulombic efficiency than that of Ni$_x$Mn$_{3-x}$O$_4$@C (x = 1) in Zn^{2+} electrolyte with Mn^{2+} additive (Figure 4b), indicating worse cycling performance. Therefore, the electrochemical performance of the assembled cells can be enhanced in the Zn^{2+} electrolyte with Mn^{2+} additive.

Figure S12. Rate performance of $Ni_xMn_{3-x}O_4@C$ (x = 0, 0.55, 0.8, 1, 1.2) electrodes at different current densities from 50 mA g^{-1} to 1200 mAg^{-1}. In the case of $Ni_xMn_{3-x}O_4@C$ (x = 1), the discharge capacity is 139.7 mAh g^{-1} at 50 mAg^{-1}. As the current density increases, the reversible capacities are 136.4, 133.6, 130.5, 125.7, 118.9, 109.6, and 95.9

mAh g^{-1} at 100, 200, 400, 600, 800, 1000, and 1200 mA g^{-1}, respectively. When the current density returns to 50 mA g^{-1}, the capacity reaches 138.8 mAg^{-1}, which is close to its original value. Reversible capacities of 137.7 mAh g^{-1}, 135.5 mAh g^{-1}, 134.3 mAh g^{-1}, and 133.1 mAh g^{-1} are delivered at 50 mA g^{-1} by Ni$_x$Mn$_{3-x}$O$_4$@C (x = 1.2), Ni$_x$Mn$_{3-x}$O$_4$@C (x = 0.8), Ni$_x$Mn$_{3-x}$O$_4$@C (x = 0), Ni$_x$Mn$_{3-x}$O$_4$@C (x = 0.55), and they drop quickly at subsequent current densities, which indicates that the rate performance of Ni$_x$Mn$_{3-x}$O$_4$ can be significantly enhanced by adjusting the morphology and carbon modification.

Figure S13. Charge-discharge profiles of Ni$_x$Mn$_{3-x}$O$_4$@C (x = 1) at 400 mA g^{-1} after different cycles. The initial discharge cures show low capacity, which is related to the initial activation of the electrode. Subsequently, the capacity of the Ni$_x$Mn$_{3-x}$O$_4$@C (x =

1) electrode decreases slowly with an obvious plateau. Moreover, the discharge capacity is 138.9 mAh g^{-1} at 400 mA g^{-1} after 150 cycles, which is close to the delivered capacity since the finish of the activation process, showing excellent cyclability compared other samples.
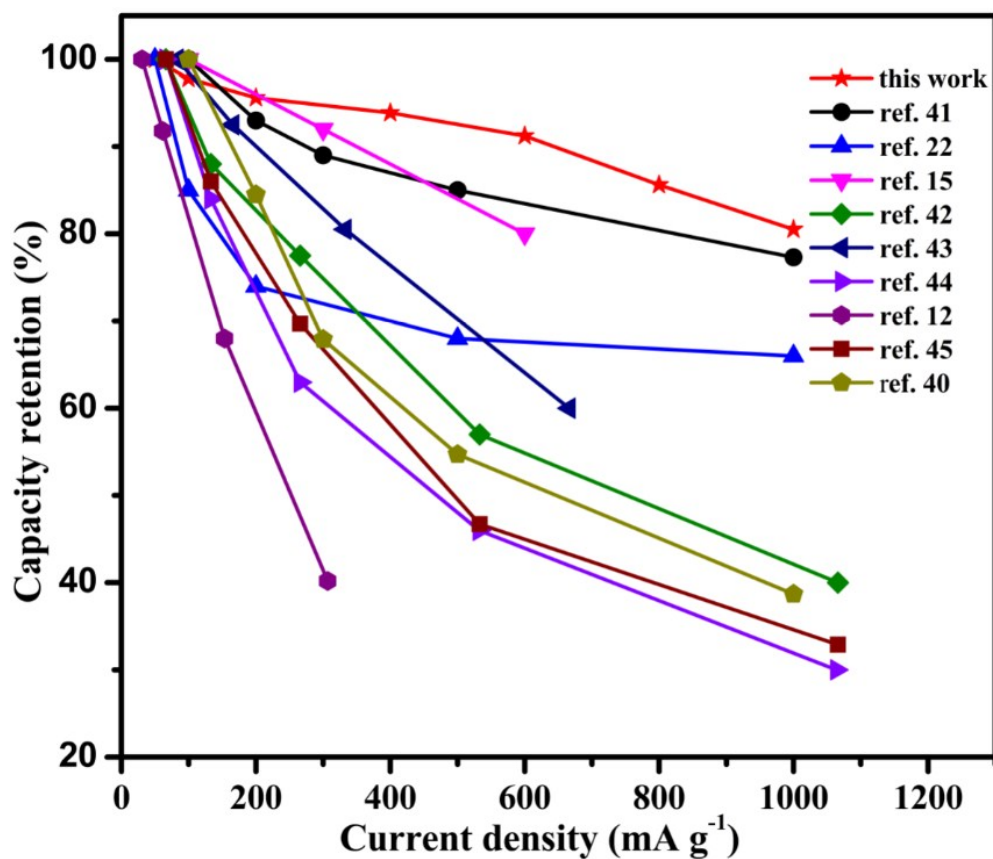
Figure S14. Capacity retention of Ni$_x$Mn$_{3-x}$O$_4$@C ($x = 1$) electrode at various current densities in comparison to the reported Mn-based materials for ZIBs.
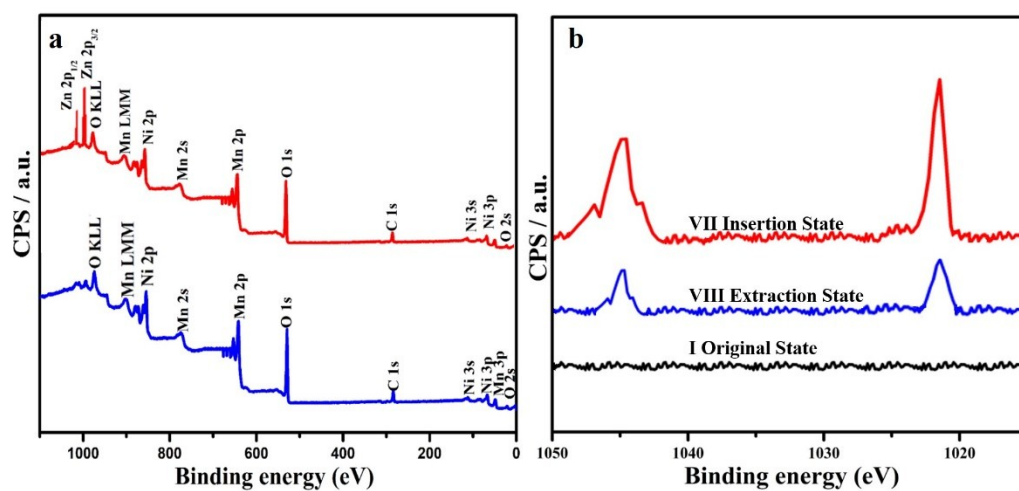
Figure S15. a) XPS spectra of $Ni_xMn_{3-x}O_4@C$ ($x = 1$) electrodes in the original and insertion states. b) Zn 2p core level spectra of $Ni_xMn_{3-x}O_4@C$ ($x = 1$) cathodes in the original, extraction, and insertion states.
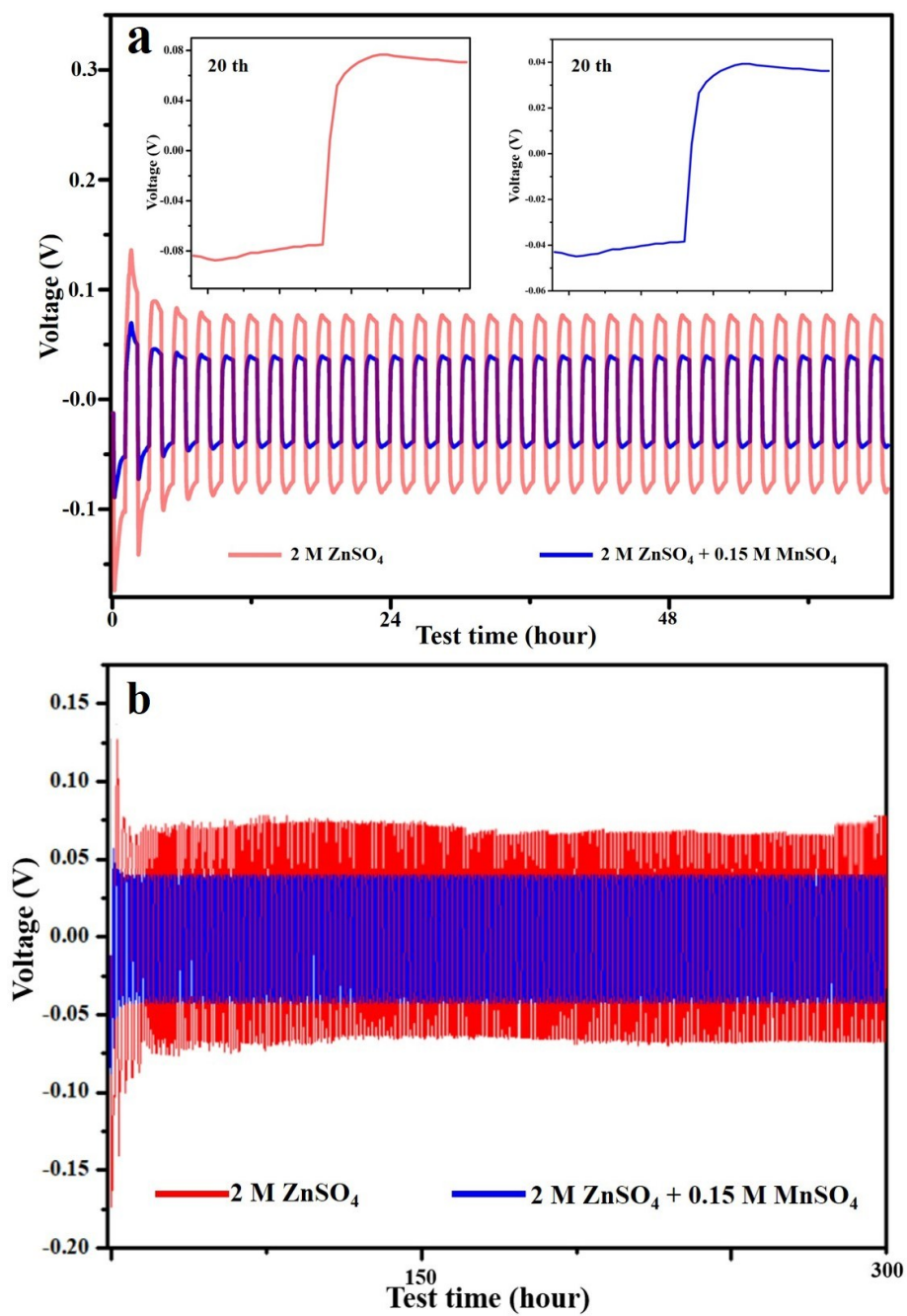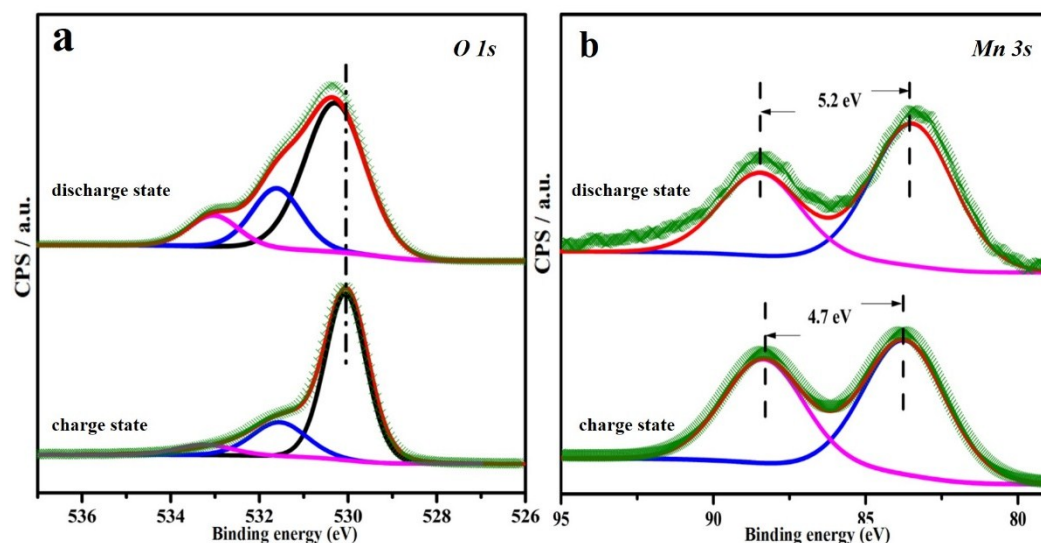
Figure S16. a) Galvanostatic cycling of Zn/Zn symmetrical cells at 0.1 mA cm⁻² in 2 M

ZnSO$_4$ and 2 M ZnSO$_4$ + 0.15 M MnSO$_4$ electrolytes. Insets shows the enlarged voltage profiles of the 20th cycles for the two electrolytes. b) Long-term cycling performance of Zn/Zn symmetrical cells in 2 M ZnSO$_4$ and 2 M ZnSO$_4$ + 0.15 M MnSO$_4$ electrolytes

Figure S17. XPS spectra of O 1s and Mn 3s for Ni$_x$Mn$_{3-x}$O$_4$@C (x =1) after discharge/charge. Meanwhile, O 1s spectra of Ni$_x$Mn$_{3-x}$O$_4$@C (x =1) are different between the charge state and the discharge state. The positive shift of stronger peak at 530.1 eV can be attributed to the intercalation of Zn^{2+} into the sample during discharge. The Mn 3s spectra contain two peaks that are separated by 5.2 eV after discharge [46], indicating the reduction of Mn^{4+} to Mn^{3+}. The Mn 3s spectra contain two peaks that are separated by 4.7 eV after charge, which reflects the oxidation of Mn^{3+} to Mn^{4+} [47] and the extraction of Zn^{2+} from the sample.
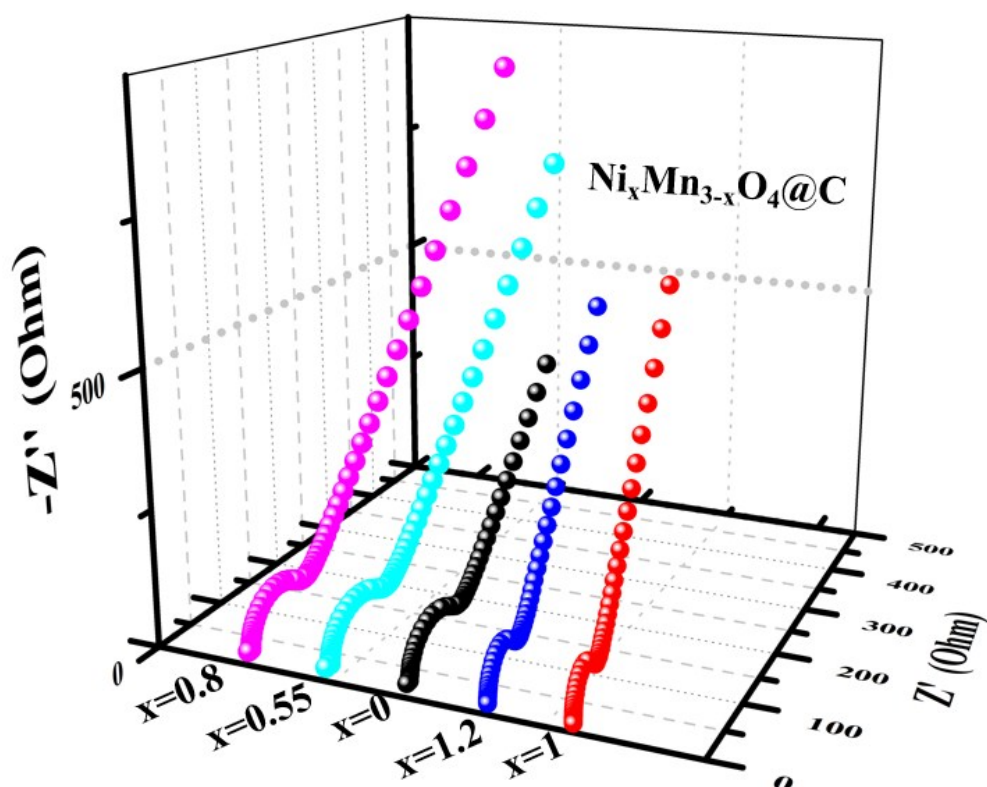
Figure S18. Nyquist plots of $Ni_xMn_{3-x}O_4@C$ (x = 0, 0.55, 0.8, 1, 1.2) electrodes after cycling at 250 mA g^{-1}. Notably, the R_{ct} value of $Ni_xMn_{3-x}O_4@C$ (x = 1) is much smaller than those of $Ni_xMn_{3-x}O_4@C$ (x = 0, 0.55, 0.8, 1.2) electrodes, manifesting a high electric conductivity that benefits from the Ni-doping in the crystalline structure, which is consistent with the low band-gap according to the density functional theory calculations.
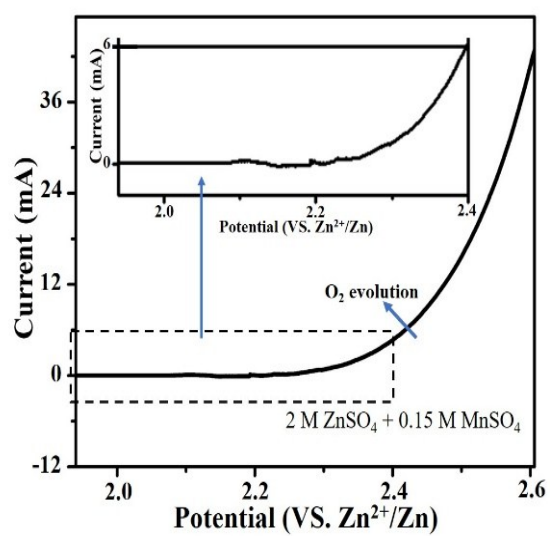
Figure S19. Electrochemical stability of $Ni_xMn_{3-x}O_4@C$ ($x = 1$) electrode in aqueous 2 M $ZnSO_4$ + 0.15 M $MnSO_4$ electrolyte. The anodic process for the electrolyte above 2.15 V can be assigned to the oxygen evolution.

a	b	c	d	e
1Ni-Oct	**1Ni-Tetr**	**2Ni-Oct**	**1Ni-Oct-1Ni-Tetr**	**2Ni-Tetr**
0 eV	**0.6 eV**	**0 eV**	**0.42 eV**	**2.16 eV**
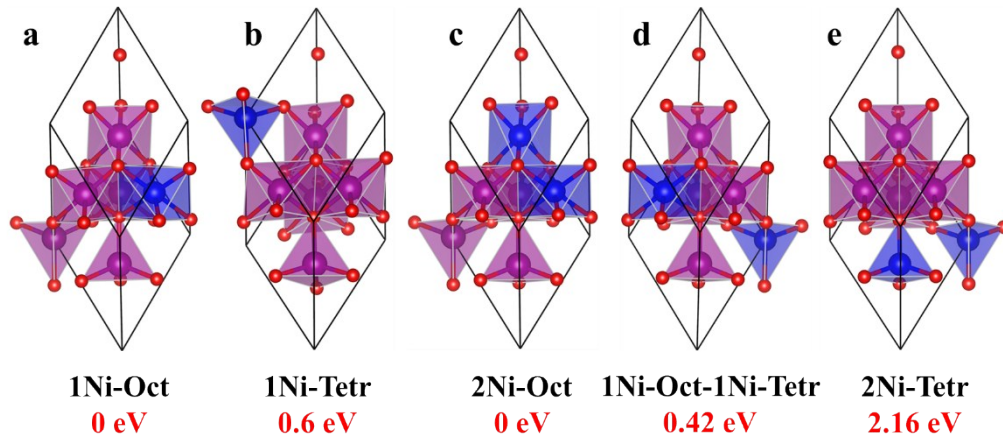
Figure S20. The relative energies for different configurations of $Ni_xMn_{3-x}O_4$, when Ni atoms are doped to the A-sites or the B-sites. a) One Ni atom is doped to the B-site (0 eV, more favorable) in the $NiMn_5O_8$, while one Ni atom is doped to the A-site (0.6 eV) in the $NiMn_5O_8$ in (b). c) Two Ni atoms are all doped to the B-sites (0 eV, more favorable) in the $Ni_2Mn_4O_8$. d) One Ni atom is doped to the B-site and the other one is doped to the A-site (0.42 eV) in the $Ni_2Mn_4O_8$. e) Two Ni atoms are all doped to the A-sites (2.16 eV) in the $Ni_2Mn_4O_8$. According to the relative energies, it is found that Ni atoms prefer to locate at the B-sites.

Table S1. Binding energy and peak area of $Ni_xMn_{3-x}O_4@C$ ($x = 1$) compound calcined at different temperature.

T(°C)	Binding Energy (eV)			Area (%)		
	Mn^{2+}	Mn^{3+}	Mn^{4+}	Mn^{2+}	Mn^{3+}	Mn^{4+}
365 °C	641	642.6	643.6	14.8	50.4	34.8
410 °C	641.4	642.5	643.5	10.7	68.9	20.4
455 °C	641.3	642.5	643.5	14.5	5.2	80.3
500 °C	641.4	642.3	643.5	20.3	17.1	62.6

Table S2. Summary of electrochemical performance of typical cathode materials for ZIBs

Cathode materials	Publication data (Month Year)	Electrolyte	Cycling performance	Ref.
amorphous α-MnO_2	December 2011	1 M $ZnSO_4$	100 mAh g^{-1} at 105 mA g^{-1} after 100 cycles	[13]
α-MnO_2 nanorod	April 2015	1 M $ZnSO_4$	140 mAh g^{-1} at 42 mA g^{-1} after 30 cycles	[14]
α-MnO_2 nanorod	April 2016	2 M $ZnSO_4$ and 0.1 M $MnSO_4$	260 mAh g^{-1} at 308 mA g^{-1} after 60 cycles	[15]
Todorokite-type MnO_2	September 2013	1 M $ZnSO_4$	98 mAh g^{-1} at 50 mA g^{-1} after 50 cycles	[16]
$Zn_3[Fe(CN)_6]_2$	January 2015	1 M $ZnSO_4$	81 mAh g^{-1} at 60 mA g^{-1} after 100 cycles	[17]
$Cu_3[Fe(CN)_6]_2$	December 2014	20 mM $ZnSO_4$	52 mAh g^{-1} at 60 mA g^{-1} after 100 cycles	[18]

β-MnO$_2$	December 2017	3 M Zn(CF$_3$SO$_3$)$_2$ + 0.1 M Mn(CF$_3$SO$_3$)$_2$	225 mAh g^{-1} at 136 mA g^{-1} after 100 cycles	[19]
Mesoporous γ-MnO$_2$	May 2015	1 M ZnSO$_4$	150 mAh g^{-1} at 0.5 mA cm^{-2} after 100 cycles	[20]
Zn$_{0.25}$V$_2$O$_5$•nH$_2$O nanobelts	August 2016	1 M ZnSO$_4$	260 mAh g^{-1} at 2.4 A g^{-1} after 500 cycles	[21]
Spinel-ZnMn$_{1.86}$O$_4$	September 2016	3 M Zn(CF$_3$SO$_3$)$_2$	150 mAh g^{-1} at 50 mA g^{-1} after 50 cycles	[22]
Na$_3$V$_2$(PO$_4$)$_3$	May 2016	0.5 M Zn(CH$_3$COO)$_2$	108 mAh g^{-1} at 100 mA g^{-1} after 200 cycles	[23]
zinc orthovanadate	August 2018	1 M Zn(TFSI)$_2$ + 20 M LiTFSI	125 mAh g^{-1} at 2000 mA g^{-1} after 800 cycles	[24]
SSWM@Mn$_3$O$_4$	April 2018	2 M ZnSO$_4$ and 0.1 M MnSO$_4$	296 mAh g^{-1} at 100 mA g^{-1} after 500 cycles	[25]
V$_{10}$O$_{24}$·12H$_2$O	October 2018	3 M Zn(CF$_3$SO$_3$)$_2$	98 mAh g^{-1} at 10 A g^{-1} after 500 cycles	[26]
K$_2$V$_8$O$_{21}$	July 2018	2 M ZnSO$_4$	126 mAh g^{-1} at 6 A g^{-1} after 300 cycles	[27]
Na$_{0.33}$V$_2$O$_5$	January 2018	3 M Zn(CH$_3$F$_3$SO$_3$)$_2$	367.1 mAh g^{-1} at 100 mA g^{-1} after 100 cycles	[28]
V$_2$O$_5$	April 2018	3 M ZnSO$_4$	121 mAh g^{-1} at 1000 mA g^{-1} after 400 cycles	[29]
KMn$_8$O$_{16}$	August 2018	1 M ZnSO$_4$ + 0.3 M K$_2$SO$_4$	77 mAh g^{-1} at 100 mA g^{-1} after 100 cycles	[30]
Na$_{1.1}$V$_3$O$_{7.9}$ nanoribbons/graphene	July 2018	1 M Zn(CF$_3$SO$_3$)$_2$	84.8 mAh g^{-1} at 1000 mA g^{-1} after 500 cycles	[31]
H$_2$V$_3$O$_8$ Nanowire/Graphene	March 2018	3 M Zn(CF$_3$SO$_3$)$_2$	336 mAh g^{-1} at 100 mA g^{-1} after 150 cycles	[32]
3D MnO$_x$@C	December	0.75 M Na$_2$SO$_4$	60 mAh g^{-1} at	[33]

		er 2017	+ 0.25 M ZnSO$_4$	2000 mA g^{-1} after 1000 cycles	
Na$_2$V$_6$O$_{16}$·3H$_2$O barnesite	March 2018	1 M ZnSO$_4$	228 mAh g^{-1} at 5400 mA g^{-1} after 300 cycles	[34]
ZnMn$_2$O$_4$/Mn$_2$O$_3$	October 2018	1 M ZnSO$_4$	111.9 mAh g^{-1} at 500 mA g^{-1} after 300 cycles	[35]
Mo$_6$S$_8$	May 2016	1.1 M ZnSO$_4$	55 mAh g^{-1} at 600 mA g^{-1} after 350 cycles	[36]
Al-doped VO$_{1.52}$(OH)$_{0.77}$	April 2017	1 M ZnSO$_4$	105 mAh g^{-1} at 15 mA g^{-1} after 50 cycles	[37]
Zn$_x$Mo$_6$S$_8$	March 2016	0.1 M ZnSO$_4$	88 mAh g^{-1} at 6.4 mA g^{-1} after 20 cycles	[38]
Layered VS$_2$ Nanosheet	January 2017	1 M ZnSO$_4$	110.9 mAh g^{-1} at 500 mA g^{-1} after 200 cycles	[39]
Manganese Sesquioxide	January 2017	2 M ZnSO$_4$	82.2 mAh g^{-1} at 2 A g^{-1} after 1000 cycles	[40]
Ni$_x$Mn$_{3-x}$O$_4$@C	---	2 M ZnSO$_4$ + 0.15 M MnSO$_4$	131 mAh g^{-1} at 400 mA g^{-1} after 850 cycles	This wok

References

[1] W. Kohn, L. Sham, *Phys. Rev.,* 1965, **140**, A1133-A1138.

[2] P. Blöchl, *Phys. Rev. B,* 1994, **50**, 17953-17979.

[3] G. Kresse, D. Joubert, *Phys. Rev. B,* 1999, **59**, 1758-1775.

[4] G. Kresse, J. Furthmüller, *Phys. Rev. B,* 1996, **54**, 11169-11186.

[5] G. Kresse, J. Furthmüller, *Comp. Mater. Sci.,* 1996, **6**, 15-50.

[6] J. Perdew, K. Burke, M. Ernzerhof, *Phys. Rev. Lett.,* 1996, **77**, 3865-3868.

[7] S. Hirai, Y. Goto, Y. Sakai, A. Wakatsuki, Y. Kamihara, M. Matoba, *J. Phys. Soc. Jpn.,* 2015, **84**, 114702.

[8] C. Franchini, R. Podloucky, J. Paier, M. Marsman, G. Kresse, *Phys. Rev. B,* 2007, **75**, 195128

[9] J. Huang, H. Hsu, C. Cheng, *J. Magn. Magn. Mater.,* 2014, **358**,149.

[10] T. Larbi, M. Lakhdar, A. Amara, B. Ouni, A. Boukhachem, A. Mater, M. Amlouka, *J. Alloy. Compd.,* 2015, **626**, 93-101.

[11] J. Wang, J. Zhang, *J. Mater. Res.,* 2012, **27**, 928-931.

[12] S. Han , S. Kim, D. Li, V. Petkov, H. Yoo, P. Phillips, H. Wang, J. Kim , K. More, B. Key, R. Klie, J. Cabana, V. Stamenkovic, T. Fister, N. Markovic, A. Burrell, S. Tepavcevic, J. Vaughey, *Chem. Mater.,* 2017**, 29**, 4874-4884.

[13] C. Xu, B. Li, H. Du, F. Kang, *Angew. Chem. Int. Ed.,* 2012, **51**, 933-935.

[14] B. Lee , H. Lee , H. Kim , K. Chung, B. Cho, S. Oh, *Chem. Commun.,* 2015, **51**, 9265-9268.

[15] H. Pan, Y. Shao, P. Yan, Y. Cheng, K. Han, Z. Nie, C. Wang, J. Yang, X. Li, P. Bhattacharya, K. Mueller, J. Liu, *Nat. Energy,* 2016, **1**, 16039.

[16] J. Lee, J. Ju, W. Cho, B. Cho, S. Oh, *Electrochim. Acta,* 2013, **112**, 138-143.

[17] L. Zhang, L. Chen, X. Zhou, Z. Liu, *Adv. Energy Mater.,* 2015, **5**, 1400930.

[18] R. Trócoli, F. Mantia, *ChemSusChem,* 2015, **8**, 481-485.

[19] N. Zhang, F. Cheng, J. Liu, L. Wang, X. Long, X. Liu, F. Li, J. Chen, *Nat. commun.,* 2017, **8**, 405.

[20] M. Alfaruqi, V. Mathew, J. Gim, S. Kim, J. Song, J. Baboo, S. Choi, J. Kim, *Chem. Mater.,* 2015, **27**, 3609-3620.

[21] D. Kundu, B. Adams, V. Duffort, S. Vajargah, L. Nazar, *Nat. Energy,* 2016, **1**, 16119.

[22] N. Zhang, F. Cheng, Y. Liu, Q. Zhao, K. Lei, C. Chen, X. Liu, J. Chen, *J. Am. Chem. Soc.,* 2016, **138**, 12894-12901.

[23] G. Li, Z. Yang, Y. Jiang, C. Jin, W. Huang, X. Ding, Y. Huang, *Nano Energy,* 2016, **25**, 211-217.

[24] D. Chao, C. Zhu, M. Song, P. Liang, X. Zhang, N. Tiep, H. Zhao, J. Wang, R. Wang, H. Zhang, H. Fan, *Adv. Mater.,* 2018, **30**, 1803181.

[25] C. Zhu, G. Fang, J. Zhou, J. Guo, Z. Wang, C. Wang, J. Li, Y. Tang, S. Liang, *J. Mater. Chem. A,* 2018, **6**, 9677-9683.

[26] T. Wei, Q. Li, G. Yang, C. Wang, *Electrochim. Acta,* 2018, **287**, 60-67.

[27] B. Tang, G. Fang, J. Zhou, L. Wang, Y. Lei, C. Wang, T. Lin, Y. Tang, S. Liang, *Nano Energy,* 2018, **51**, 579.

[28] P. He, G. Zhang, X. Liao, M. Yan, X. Xu, Q. An, J. Liu, L. Mai, *Adv. Energy Mater.,* 2018, **8**, 1702463.

[29] J. Zhou, L. Shan, Z. Wu, X. Guo, G. Fang, S. Liang, *Chem. Commun.,* 2018, **54**, 4457-4460.

[30] J. Cui, X. Wu, S. Yang, C. Li, F. Tang, J. Chen, Y. Chen, Y. Xiang, X. Wu, Z. He, *Front. Chem.,* 2018, **6**, 352.

[31] Y. Cai, F. Liu, Z. Luo, G. Fang, J. Zhou, A. Pan, S. Liang, *Energy Storage Mater.,* 2018, **13**, 168-174.

[32] Q. Pang, C. Sun, Y. Yu, K. Zhao, Z. Zhang, P. Voyles, G. Chen, Y. Wei, X. Wang, *Adv. Energy Mater.,* 2018, **8**, 1800144.

[33] J. Ko, M. Sassin, J. Parker, D. Rolison, J. Long, *Sustainable Energy Fuels,* 2018, **2**,

626-636.

[34] V. Soundharrajan, B. Sambandam, S. Kim, M. Alfaruqi , D. Putro, J. Jo, S. Kim, V. Mathew, Y. Sun, J. Kim, *Nano Lett.,* 2018, **18**, 2402-2410.

[35] S. Yang, M. Zhang, X. Wu, X. Wu, F. Zeng, Y. Li, S. Duan, D. Fan, Y. Yang, X. Wu, *J. Electroanal. Chem.,* 2019, **832**, 69-74.

[36] Y. Cheng, L. Luo, L. Zhong, J. Chen, B. Li, W. Wang, S. Mao, C. Wang, V. Sprenkle, G. Li, J. Liu, *ACS Appl. Mater. Inter.,* 2016, **8**, 13673-13677.

[37] J. Jo, Y. Sun, S. Myung, *J. Mater. Chem. A,* 2017, **5**, 8367-8375.

[38] M. Chae, J. Heo, S. Lim, S. Hong, *Inorg. Chem.,* 2016, **55**, 3294-3301.

[39] P. He, M. Yan, G. Zhang, R. Sun, L. Chen, Q. An, L. Mai, *Adv. Energy Mater.,* 2017, **7**, 1601920.

[40] B. Jiang, C. Xu, C. Wu, L. Dong, J. Li, F. Kang, *Electrochim. Acta,* 2017, **229**, 422-428.

[41] Y. Fu, Q. Wei, G. Zhang, X. Wang, J. Zhang, Y. Hu, D. Wang, L. Zuin, T. Zhou, Y. Wu, S. Sun, *Adv. Energy Mater.,* 2018, **8**, 1801445.

[42] M. Alfaruqi, J. Gim, S. Kim, J. Song, J. Jo, S. Kim, V. Mathew, J. Kim, *J. Power Sources,* 2015, **288**, 320-327.

[43] M. Alfaruqi, J. Gim, S. Kim, J. Song, D. Pham, J. Jo, Z. Xiu, V. Mathew, J. Kim, *Electrochem. Commun.,* 2015, **60**, 121-125.

[44] M. Alfaruqi, S. Islam, V. Mathew, J. Song, S. Kim, D. Tung, J. Jo, S. Kim, J. Baboo, Z. Xiu, *Appl. Surf. Sci.,* 2017, **404**, 435-442.

[45] M. Alfaruqi, S. Islam, J. Gim, J. Song, S. Kim, D. Pham, J. Jo, Z. Xiu, V. Mathew, J. Kim, *Chem. Phys. Lett.,* 2016, **650**, 64-68.

[46] R. Kalubarme, H. Jadhav, H. Park, *Electrochim. Acta*, 2013, **87**, 457-465.

[47] M. Chigane, M. Ishikawa, *J. Electrochem. Soc.*, 2000, **147**, 2246-2251.